Dalton Transactions

Accepted Manuscript

ROYAL SOCIETY OF CHEMISTRY

www.rsc.org/dalton

Journal Name

ARTICLE

Atomic and electronic structure transformations in SnS_2 at high pressures: A joint single crystal X-ray diffraction and DFT study

M. Ø. Filsø[a], E. Eikeland[a], J. Zhang[a], S. R. Madsen[a], B. B. Iversen[a]

Received 00th January 20xx,
Accepted 00th January 20xx

DOI: 10.1039/x0xx00000x

www.rsc.org/

The layered semiconductor SnS_2 spurs much interest for both intercalation and optoelectronic applications. Despite the wealth of research in the field of metal dichalcogenides, the structure-property relationship of this compound remains unclear. Here we present a thorough study combining single-crystal X-ray diffraction and DFT calculations on SnS_2 in the pressure range $0 < p < 20$ GPa. The anisotropic compression of the unit cell is clearly linked to the van der Waals interactions between the S-Sn-S sandwich layers, as the compression mainly affects the interlayer distance. This compression behavior is coincidal with the compression of other well-known layered compounds (graphite and boron nitride) but differs significantly from the compression of other MS_2 compounds, making it clear that SnS_2 presents a unique and interesting case in the field of metal dichalcogenides. The compression leads to a significant increase in S…S interlayer interaction which in turn results in a change in the electronic structure, documented through DFT band structure calculations. The calculated narrowing of the band gap is supported by a significant, reversible color change of the single crystal. At 20 GPa, the size of the band gap has decreased from 2.15 to 0.88 eV, and band gap closure is predicted to occur at 33 GPa.

Introduction

Interest in metal dichalcogenides MX_2, X = S, Se has increased dramatically over the past few decades as a result of their versatile structure and properties. The layered structure consists of X-M-X sandwich layers, which enables a variety of intercalation applications, e.g. Li-intercalation for lithium ion batteries.[1-5] Furthermore, their promising optical properties open up the possibility for optoelectronic and photocatalytic applications. [6-11] Understanding the structure of metal dichalcogenides is therefore of great importance such that their properties may be tuned to meet technological demands.

High-pressure techniques can be utilized to relate the structure of this essential group of compounds to their physical properties. The act of forcing atoms closer together offers pivotal insight into the nature of the interatomic interactions which are the very key to the properties of the compound. In a layered structure such as MX_2, two types of interactions are present: strong, polar covalent intralayer X-M bonds and weak X…X van der Waals interactions. As a result of their soft nature, the van der Waals interactions are more easily manipulated and may therefore be easily probed by gradually exposing the compounds to increased pressure. Information concerning the van der Waals X…X interlayer interactions is important to fully understand the properties of the material,[12-14] and gaining this information will benefit not only research in layered dichalcogenides, but also the general research of the nature of van der Waals interactions.

In this article, we will focus on the simple 2H polytype of SnS_2, space group $P\bar{3}m1$, with Sn at (0,0,0) and S at (2/3,1/3,z), $z \sim 0.25$, see Figure 1.[15] SnS_2 is a semiconductor, and the indirect band gap of the 2H polytype is 2.2 eV, in the visible range of the electromagnetic spectrum.[16, 17] The high-pressure behavior of SnS_2 has been studied by single-crystal X-ray diffraction (SCXRD) up to 3 GPa,[18] in a joint powder X-ray diffraction and theoretical study up to 10 GPa,[19] and by Raman spectroscopy up to 20 GPa.[20, 21] Early studies of optical properties and band structure were performed by Powell and co-workers.[22, 23] Furthermore, a theoretical study by He *et al.* investigated the properties at pressures $0 < p < 20$ GPa and temperatures $0 < T < 800$ K.[24] It is the goal of this study to expand the knowledge about the van der Waals forces present in SnS_2 and their influence on the properties of the material, both concerning the atomic and electronic structure. Therefore, a comprehensive, combined single-crystal X-ray diffraction and DFT study was performed, going to the high pressure 20(1) GPa. In addition, a thorough comparison with other layered materials will categorize the interlayer interactions of the material in the range of other prominent materials such as boron nitride, graphite, and other MS_2 compounds. An improved understanding of weak van der Waals-type interactions will benefit in a wide range of scientific areas, since these interactions are part of the structure of many prominent materials used in society today.

Experimental

Synthesis

[a] *Center for Materials Crystallography, Department of Inorganic Chemistry and iNANO, Aarhus University (DK)*

Electronic Supplementary Information (ESI) available: [details of any supplementary information available should be included here]. See DOI: 10.1039/x0xx00000x

For synthesis and crystal growth, the method of Kourtakis *et al.* was employed.[25] A mixture of 0.7265 g S and 1.2779 g Sn was loaded into one end of a 1.5 cm wide quartz ampoule, which was evacuated and sealed to a length of 15 cm. The sample was pre-reacted in a horizontal tube furnace at 600 °C for 24 hours. To prevent any vapor transport during the pre-reaction, the empty end of the ampoule was kept at higher temperature (~730 °C), utilizing the inherent heat gradient in the oven.

After pre-reaction, the ampoule was turned around so the temperature was 650 °C at the sample end and 600 °C at the empty end. The sample recrystallized in the 'cold' end of the ampoule under these conditions for 10 days, after which it was furnace-cooled to RT. The result was a mixture of µm-thin sheets several mm across and smaller, thicker plates, approximately 100x100x20 μm^3. All tested crystals were of the second type and diffracted as single crystals to large angles.

Data collection and reduction

A 93x80x20 μm^3 single crystal was selected, and data were collected at ambient pressure and temperature on a SuperNova diffractometer from Oxford Diffraction using Mo-K_α radiation, λ = 0.71073 Å. Subsequently, the crystal was mounted in a Boehler-Almax-type DAC with 600 µm culets. A 200 µm thick steel plate was indented to a thickness of 120 µm. A 177±13 µm hole was made by spark erosion. The pressure medium used was a 4:1 mixture of methanol/ethanol which is hydrostatic to ~9.5 GPa.[26, 27]

High-pressure data were collected on a Bruker-Nonius APEX diffractometer equipped with an Ag-K_α source, λ = 0.56086 Å. Both data collection strategies (ambient and high-pressure) are attached in the supporting information (Tables S1 and S2). Due to the plate-like morphology of the crystals, the preferred orientation of the crystal on the diamond culet was with the *c*-axis perpendicular to the culet. This orientation combined with the limited angular window available for incoming and outgoing radiation lead to poor completeness (approx. 33 % for the complete data range) for all high-pressure datasets. Throughout the pressure range, the scattering power of the crystal was high (max. 2θ ≈ 50°). Data coverage and R(int) values are given in Table S3.

The pressure was determined by the fluorescent signal from two rubies, which were included at different positions inside the pressure chamber.[28] The fluorescence was measured using a green laser from Ocean Optics in a home built setup. After each pressure increase, the cell was allowed to equilibrate in pressure for at least two hours before initiating data collection. The development of the pressure during equilibration was followed through fluorescence measurements. Furthermore, the pressure was measured immediately before and after each data collection to evaluate its stability during measurement.

As the pressure increased past the hydrostatic limit of the 4:1 methanol:ethanol medium, a pressure gradient built up slowly in the pressure chamber. For data collection up to 13.7(2) GPa, all differences in pressure between the two rubies were within their standard deviation. However, as pressure increased to 14.8(2) GPa, the ruby signal broadened signi-ficantly, and the peak fitting procedure did not recover any meaningful uncertainties. After data collection at 16.8(4) GPa the DAC was heat treated at 130 °C for 2 hours to temporarily reestablish hydrostatic conditions as this is likely to reduce the pressure gradient.[29] After heat treatment and subsequent cooling to RT, a significant pressure drop was observed. Increasing the pressure to 20(1) GPa, the pressure difference was further increased, making it clear that establishing quasihydrostatic conditions at these high pressures was not feasible. A final dataset was collected at this pressure. No further heat treatment was attempted.

The frames were integrated with SAINT and corrected for absorption through a multi-scan procedure in SADABS. Furthermore, absorption by the pressure cell was taken into account with the SHADE software.[30, 31] During the integration, the box size was fixed to values suitable for the sample peak profile to avoid bias from the larger and more intense diamond reflections. The structure was solved using SHELXS and refined using SHELXL as implemented in the program OLEX2.[32] Reflections with poor statistics were omitted from the structure refinements. As a result of the high symmetry of the crystal structure and the great scattering power, refinement progressed without major issues in spite of the low completeness. An anisotropic refinement of the ADPs resulted in highly elongated ellipsoids for both S and Sn along the *c* direction. This effect was concluded to be a result of the orientation of the crystal in the DAC which leads to poor sampling in the (0, 0, *l*) direction of reciprocal space. Since errors often accumulate in the refinement of thermal vibrations, the effect of the low completeness was only evident in the ADPs, and an isotropic model for thermal vibration was maintained through all refinements. In a standard high-pressure study, it is normal to observe a decrease in the ADP magnitude with increasing pressure. However, this trend is not apparent in this case, presumably due to low completeness and strain effects. Therefore, no structural interpretation is drawn from the ADPs. Selected parameters from refinement can be found in Table S4.

Theoretical calculations

Density Functional Theory (DFT) calculations were carried out using the projector augmented-wave (PAW) method[33] as implemented in the Vienna *ab initio* simulation package (VASP).[34] The PBE functional was used for crystal structure relaxation.[35] TB-mBJ exchange-correlation potentials[36] were used in the electronic structure calculation. Van der Waals interactions were taken into account during structural relaxation at the vdW-DF level with optB86b as the exchange functional (optB86b-vdW).[37] In the current work the spin-orbit coupling was not included. The plane-wave energy cutoff was set at 400 eV, and a 6×6×4 Monkhorst-Pack k mesh was used for crystal structure optimization, while a larger 15×15×10 Monkhorst-Pack k mesh was used for electronic structure calculations. An energy convergence criterion of 10^{-6} eV and a Hellmann-Feynman force convergence criterion of 0.001 eV Å-1 were adopted.

Results and discussion

Selected crystal structure results from the high-pressure SCXRD data collections are given in Table 1. The contraction of the unit cell is highly anisotropic over the whole pressure range, Figure 2a. At 20(1) GPa, the compression of the *a*-axis is 3.79(2) % while the compression of the *c*-axis is 15.53(7) %. At pressures above 12 GPa, the theoretical and experimental results differ, displaying the effect of the non-hydrostatic conditions which is not included in the DFT model, leading to a slightly more anisotropic compression behavior in the experi-ment. It should be mentioned that a similar difference be-tween experiment and calculation was observed in the com-pression of the structurally closely related MoS_2 compound. Here, the difference was found to be caused by a layer sliding mechanism.[38] Further investigation is needed in order to fully confirm or disprove if this is also the case for SnS_2.

Comparing the unit cell compression to the previous studies of SnS_2, the present results agree well with the results by Knorr *et al.*[19] However, the compression of the *c*-axis as estimated by Hazen and Finger[18] is significantly larger, see Figure S1 in the Supporting Information. This deviation can likely be attributed to compression under non-hydrostatic conditions in the work of Hazen and Finger, as the pressure medium used (glycerin) has a low hydrostatic limit of 1.4 GPa.[27] The larger compression along *c* is in line with the effect of non-hydrostatic conditions observed in our study at pres-sures above 12 GPa.

A comparison of the unit cell axis compression with other layered structures is displayed in Figure 2b. In all cases, *a* is the unit cell axis parallel to the atomic layers and *c* is oriented perpendicular to the layers. The compression of the *c*-axis agrees very well with the compression of boron nitride, BN, and graphite.[39] It is clear from this similarity that the nature of the compression of SnS_2 is mainly compression against van der Waals forces. Therefore, the compression of the covalently bonded S-Sn-S sandwich layers must be minimal compared to the compression of the interlayer. This conclusion is supported by calculations of layer thickness and interlayer distance parallel to *c* as a function of pressure, which show a nearly constant layer thickness and a greatly decreasing interlayer distance, see Figure S2. The compression of the interlayer S…S distance is 19.8(3) % at 20(1) GPa. It is curious that the very related structure of MoS_2[40] (space group $P6_3/mmc$) displays significantly lower compressibility along *c*. Investigating other MS_2 structures, WS_2[41] (isostructural with MoS_2) and TiS_2[42] (isostructural with SnS_2), shows that SnS_2 is the outlier in this respect. The smaller compressibility of these other MS_2 compounds is likely a result of a stronger interaction between layers, leaving SnS_2 as the only disulfide of this group which expresses pure van der Waals-type S…S interactions directly comparable to the interlayer forces in graphite.

A comparison with portlandite, $Ca(OH)_2$ (space group $P\bar{3}m1$) indicates the effect of interlayer H-bonding which causes a more linear compression of the *c*-axis until a balance between the attractive forces of the H-bond and the repulsive O…O interactions is established.[43]

For compression along *a*, the curve for SnS_2 falls between the curves of MoS_2 and TiS_2, following the trend that the more covalent bond is the least compressible and vice versa. All MS_2 structures are significantly more compressible than BN and graphite, owing to the larger compressibility of the M-S bond compared with the stronger sp^2 C-C/B-N bond. Furthermore, for SnS_2 a regularization of the SnS_6 octahedra is observed as the Sn-S-Sn angle decreases from 90.80(7)° at ambient pressure to 89.97(17)° at 20(1) GPa. This change contributes to the compression along *a*. This subtle effect was predicted earlier by Knorr *et al.*,[19] but never proven experimentally. The change in the octahedral angle is more pronounced in the related structure of portlandite, $Ca(OH)_2$, where the O-Ca-O angle decreases from 98.7(2)° at 0.5 GPa to 95.8(3)° at 9.7 GPa.[43] The large change in angle leads to a higher compressi-bility along *a* compared to SnS_2, even though the compression of the Ca-O bond (1.3(4) % from 0.5 to 9.7 GPa) is smaller than the compression of the Sn-S bond (2.1(3) % from 0.664(9) to 9.78(8) GPa).

The compression of the interlayer distance increases the S…S interaction. The Pauling crystallographic van der Waals radius for S(-II) is 1.85 Å which leads to a van der Waals contact distance of 2 x 1.85 Å = 3.70 Å. At ambient pressure the S…S distance is 3.647(3), or just below the van der Waals contact distance. With pressure, the distance decreases, reaching a value of 2.926(10) Å at 20(1) GPa. This short distance clearly induces a high degree of interaction, although a distance close to the typical S-S bond length of 2.05 Å has not been reached. The close S…S contact can be displayed by calculating the Hirshfeld surface of S mapped with d_{norm} (defined by Spackman and co-workers, see e.g. CrystEng-Comm[44]). Any red area of the Hirshfeld surface marks the overlap of van der Waals radii of the center atom and its neighbors. At 0.664(9) GPa, the area of the Hirshfeld surface facing the other S atom is blue/white, Figure 3a. However, at 20(1) GPa the same area is bright red, Figure 3b. It is also worth noting the increase in electron density in the area directly between the S atoms when comparing the calculated procrystal isosurface (ρ_{pro} = 0.010 au) at these two pressures, Figure 3.[45] This increase in electron density in the S…S region has also been observed for MoS_2[46] and TiS_2.[47]

The average mosaicity estimated by SAINT during integration is shown in Figure 4. The orientation of the crystal in the DAC infers that the xy-mosaicity and the z-mosaicity parameters relate to mosaicity in the crystallographic *ab*-plane and along the *c*-axis, respectively. As expected, the softer *c*-direction is more vulnerable to deformation. Up to 3.4 GPa, the mosaicity drops along *c*. This pressure-annealing was also observed by Hazen and Finger.[18] From this point, the mosaicity along *c* increases steadily with pressure, most likely due to the slow introduction of microstrain in the crystal. Before the measurement at 20 GPa the DAC was heat treated, which explains the small drop in mosaicity at this pressure.

The isothermal equation of state was fitted to data for both volume and axis compression within the hydrostatic limit (p < 9.5 GPa) with the software EoSFit7,[48] Figure 2a. The order of the Birch-Murnaghan equation used was determined from P *vs.* P(obs-calc) plots, in combination with the estimated standard deviations of parameters and the weighted χ^2.[49] This lead to a 3rd-order fit to the volume and the c-axis and a 2nd-order fit to the a-axis. The K' value is larger than the previously determined

accepted range of 3.8 < K´ < 8.[50] This discrepancy has been observed in other studies on SnS_2[19] and in studies on MoS_2[51, 52] and TiS_2.[42, 53] Fixing K' to 8.0 results in a bulk modulus of K_0 = 30.2(4) and a slightly poorer fit (weighted χ^2 = 4.40 compared to 1.37 for the non-constrained fit). Since the structure is significantly anisotropic, the compression is best described by two compressibilities: $\mathcal{B}_0(\|)$ and $\mathcal{B}_0(\perp)$ for compression parallel and perpendicular to the S-Sn-S sandwich layers, respectively. All relevant results from the equations of state fits are given in Table 2, along with compressibilities from studies by Knorr *et al.* and Hazen and Finger, respectively. The present results lie in between the values of the earlier findings, however the difference is considerably larger than the stan-dard uncertainties, in spite of the comparability between the axis compression curves of the present work and the study by Knorr *et al.* This discrepancy underlines the large correlation between the bulk modulus and the first derivative. Confidence ellipses of the present work for the correlation between parameters in Table 2 are given in Figure S3 and Figure S4. The deviation from the present results of the compressibilities calculated by Hazen and Finger is expected to be caused by non-hydrostatic effects in the experiment combined with a large uncertainty (not estimated) which stems from the fit to only few data points.

During data collection, a gradual, but substantial color change of the crystal was observed, as is evident from images taken during pressurization, Figure 5. Being yellow/orange and transparent at ambient pressure, the color slowly intensified to a dark red before transitioning to black and opaque at approx. 15 GPa. Upon decompression, it was clear that the color change was fully reversible. The color change is attri-buted to a change in the electronic structure. As the layers are forced together, the band gap decreases because of the increased S…S interlayer interaction. Hence, the amount of visible light with sufficient energy to be absorbed increases. Applying a sufficiently high pressure leads to absorption of all visible light, and the crystal turns black. Unfortunately, it was not possible to measure the band gap experimentally during the experiment. The band gap calculated by DFT is shown in Figure 6. One set of calculations is based on the experimental unit cell which was not allowed to relax, while the other is a fully relaxed theoretical study. Since the PBE functional is known to overestimate the unit cell dimensions, the relaxed-structure curve is slightly shifted towards lower pressures.

The onset of band gap closure was previously proposed by Knorr *et al.* to occur at around 10 GPa through theoretical calculations using the PBE functional.[19] However, the conventional PBE functional is known to underestimate band gaps in compounds containing d-block elements. Furthermore, the van der Waals interactions were not considered. From our theoretical calculations using the mBJ potential the band gap at 0 GPa was calculated to be 1.96 eV, only ~0.24 eV below the experimentally derived value at ambient pressure. It is evident that the size of the band gap is indeed gradually decreasing in the whole pressure range. However, even at 20 GPa, the band gap retained a value of 0.88 eV. The band gap closure point was calculated to be around 33 GPa.

The orbital-projected band structure of SnS_2 is shown in Figure 7. As the interlayer distance is decreased, hybridization is enhanced between S(p_z) orbitals, causing a steep increase in the energy level of the antibonding p_z orbital (shown in red) and thereby the level of the valence band maximum. The interlayer S…S interactions thus play a significant role for the electronic properties. This finding underlines the importance of properly modeling even weak interactions.

The decrease in Sn-S bond length with increasing pressure causes an increase of S(p_x) and S(p_y) antibonding orbital energy levels, although more moderate than the increase found for S(p_z). The increase of antibonding S(p) orbitals causes an increase in the conduction band at all points except at the K point, which decreases in energy. This leads to a shift in conduction band minimum (CBM) from the L point to the K point. This effect might be a result of a decrease in contri-bution of S orbitals at the K point as a result of charge transfer from S to Sn as the layers are forced together.[46, 54] The decrease in S-orbital contribution is illustrated in Figure 7 by the decrease in thickness of the colored bands. The increase in interlayer interaction is indicated by the increase in the slope of the dispersion curves in the segment between Γ and A, which is the direction perpendicular to the layers.[14, 55]

Conclusions

A joint high-pressure single-crystal X-ray diffraction and DFT study of SnS_2 at pressures 0 < p < 20 GPa was presented, and the influence of the van der Waals interactions on the atomic structure and the electronic properties was investigated. The layered structure compresses anisotropically over the whole pressure range, where the compression in the *c*-direction stems solely from the decrease in interlayer distance. In this way, the compression of the interlayer is directly comparable to the compression of BN and graphite, in contrast to the compression of similar compounds MoS_2 and TiS_2. This significant difference has not, to our knowledge, been put forward before and indicates that the interlayer interaction in MoS_2 and TiS_2 is stronger than the typical van der Waals interaction.

The compression of the interlayer distance leads to an increased S…S interaction, which increases S(p_z) hybridization and changes the total band structure. A steady decrease of the band gap is observed, causing a color change of the crystal from yellow over red to black. No semiconductor to semimetal transition was observed in the pressure range; band gap closure is calculated to occur at approx. 33 GPa, provided no phase transitions take place between 20 and 33 GPa. It is clear that the weak van der Waals interactions play a crucial role for the properties of the material. High-quality crystallographic data or theoretical calculations including a proper modeling of these interactions (*i.e.* using the exchange functional optB86b-vdW) is therefore of great importance in order to predict properties of similar compounds.

Acknowledgements

The study was supported by the Danish National Research Foundation (Center for Materials Crystallography, DNRF93).

Notes and references

1 1. R. Lucena, F. Fresno and J. C. Conesa, *Appl. Catal. A-Gen.*, 2012, **415-416**, 111-117.
2 2. Z. Liu, H. Deng and P. P. Mukherjee, *ACS Appl. Mater. Interfaces*, 2013, **7**, 4000-4009.
3 3. J. Zai, K. Wang, Y. Su, X. Qian and J. Chen, *J. Power Sources*, 2011, **196**, 3650-3654.
4 4. J.-W. Seo, J.-T. Jang, S.-W. Park, C. Kim, B. Park and J. Cheon, *Adv. Mater.*, 2008, **20**, 4269-4273.
5 5. J. Morales, V. C. Pérez, J. Santos and J. L. Tirado, *J. Electrochem. Soc.*, 1996, **143**, 2847-2851.
6 6. A. Sanchez-Juarez, A. Tiburcio-Silver and A. Ortiz, *Thin Solid Films*, 2005, **480**, 452-456.
7 7. Y. C. Zhang, Z. N. Du, S. Y. Li and M. Zhang, *Appl. Catal. B-Environ.*, 2010, **95**, 153-159.
8 8. Y. Sun, H. Cheng, S. Gao, Z. Sun, Q. Liu, Q. Liu, F. Lei, T. Yao, J. He, S. Wei and Y. Xie, *Angew. Chem.*, 2012, **51**, 8727-8731.
9 9. W. Du, D. Deng, Z. Han, W. Xiao, C. Bian and X. Qian, *CrystEngComm.*, 2011, **13**, 2071-2076.
10 10. Y. Huang, C. Ling, X. Chen, D. Zhou and S. Wang, *RSC Adv.*, 2015, **5**, 32505-32510.
11 11. B. Radisavljevic, A. Radenovic, J. Brivio, V. Giacometti and A. Kis, *Nat. Nanotechnology*, 2011, **6**, 147-150.
12 12. H. Rydberg, M. Dion, N. Jacobson, E. Schröder, P. Hyldgaard, S. I. Simak, D. C. Langreth and B. I. Lundqvist, *Phys. Rev. Lett.*, 2003, **91**, 126402.
13 13. H. Guo, T. Yang, P. Tao, Y. Wang and Z. Zhang, *J. Appl. Phys.*, 2013, **113**, 013709.
14 14. Y. Seminovski, P. Palacios and P. Wahnón, *Thin Solid Films*, 2013, **535**, 387-389.
15 15. N. V. Podberezskaya, S. A. Magarill, N. V. Pervukhina and S. V. Borisov, *J. Struct. Chem.*, 2001, **42**, 654-681.
16 16. D. L. Greenaway and R. Nitsche, *J. Phys. Chem. Solids*, 1964, **26**, 1445-1458.
17 17. G. B. Dubrovskii, *Phys. Solid State*, 1998, **40**, 1557-1562.
18 18. R. M. Hazen and L. W. Finger, *Am. Mineral.*, 1978, **63**, 289-292.
19 19. K. Knorr, L. Ehm, M. Hytha, B. Winkler and W. Depmeier, *Phys. Stat. Sol. B*, 2001, **223**, 435-440.
20 20. S. V. Bhatt, M. P. Deshpande, V. Sathe and S. H. Chaki, *Solid State Commun.*, 2015, **201**, 54-58.
21 21. A. N. Utyuzh, Y. A. Timofeev and G. N. Stepanov, *Phys. Solid State*, 2010, **52**, 352-356.
22 22. M. J. Powell, *J. Phys. C: Solid State Phys.*, 1977, **10**, 2967-2977.
23 23. M. J. Powell, W. Y. Liang and D. J. Chadi, *J. Phys. C: Solid State Phys.*, 1978, **11**, 885-894.
24 24. X. He and H. Shen, *Physica B*, 2012, **407**, 1146-1152.
25 25. K. Kourtakis, J. DiCarlo, R. Kershaw, K. Dwight and A. Wold, *J. Solid State Chem.*, 1988, **76**, 186-191.
26 26. G. J. Piermarini, S. Block and J. D. Barnett, *J. Appl. Phys.*, 1973, **44**, 5377-5382.
27 27. R. J. Angel, M. Bujak, J. Zhao, G. D. Gatta and S. D. Jacobsen, *J. Appl. Cryst.*, 2007, **40**, 26-32.
28 28. G. J. Piermarini, S. Block, J. D. Barnett and R. A. Forman, *J. Appl. Phys.*, 1975, **46**, 2774-2780.
29 29. S. R. Madsen, N. Lock, J. Overgaard and B. B. Iversen, *Acta Cryst. B*, 2014, **70**, 595-601.
30 30. A. Dawson, D. R. Allan, S. Parsons and M. Ruf, *J. Appl. Cryst.*, 2004, **37**, 410-416.
31 31. S. Parsons, *Journal*, 2004.
32 32. O. V. Dolomanov, L. J. Bourhis, R. J. Gildea, J. A. K. Howard and H. Puschmann, *J. Appl. Cryst.*, 2009, **42**, 339-341.
33 33. P. E. Blöchl, *Phys. Rev. B*, 1994, **50**, 17953-17979.
34 34. G. Kresse and J. Furthmüller, *Phys. Rev. B*, 1996, **54**, 11169-11186.
35 35. J. P. Perdew, K. Burke and M. Ernzerhof, *Phys. Rev. Lett.*, 1996, **77**, 3865-3868.
36 36. F. Tran and P. Blaha, *Phys. Rev. Lett.*, 2009, **102**.
37 37. J. Klimes, D. R. Bowler and A. Michaelides, *Phys. Rev. B*, 2011, **83**.
38 38. L. Hromadová, R. Martonák and E. Tosatti, *Phys. Rev. B*, 2013, **87**, 144105.
39 39. R. W. Lynch and H. G. Drickamer, *J. Chem. Phys.*, 1966, **44**, 181-184.
40 40. D. Fan, J. Xu, M. Ma, J. Liu and H. Xie, *Physica B*, 2014, **451**, 53-57.
41 41. E. Selvi, Y. Ma, R. Aksoy, A. Ertas and A. White, *J. Phys. Chem. Solids*, 2006, **67**, 2183-2186.
42 42. R. Aksoy, E. Selvi, R. Knudson and Y. Ma, *J. Phys. Condens. Matter*, 2008, **21**, 025403.
43 43. T. Nagai, T. Ito, T. Hattori and T. Yamanaka, *Phys. Chem. Minerals*, 2000, **27**, 462-466.
44 44. M. A. Spackman and D. Jayatilaka, *CrystEngComm.*, 2009, **11**, 19-32.
45 45. M. J. Turner, J. J. McKinnon, D. Jayatilaka and M. A. Spackman, *CrystEngComm.*, 2011, **13**, 1804-1813.
46 46. A. P. Nayak, S. Bhattacharyya, J. Zhu, J. Liu, X. Wu, T. Pandey, C. Jin, A. K. Singh, D. Akinwande and J.-F. Lin, *Nature Commun.*, 2014, **5**, 3731.
47 47. Y. G. Yu and N. L. Ross, *J. Phys. Condens. Matter*, 2011, **23**, 055401.
48 48. R. J. Angel, J. Gonzales-Platas and M. Alvaro, *Z. Kristallogr.*, 2014, **229**, 405-419.
49 49. R. J. Angel, *Rev. Mineral. Geochem.*, 2000, **41**, 35-59.
50 50. A. M. Hofmeister, *Geophys. Res. Lett.*, 1993, **20**, 635-638.
51 51. Z.-H. Chi, X.-M. Zhao, H. Zhang, A. F. Goncharov, S. S. Lobanov, T. Kagamaya, M. Sakata and X.-J. Chen, *Phys. Rev. Lett.*, 2014, **113**, 036802.
52 52. R. Aksoy, Y. Ma, E. Selvi, M. C. Chyu, A. Ertas and A. White, *J. Phys. Chem. Solids*, 2006, **67**, 1914-1917.

53 53. F. Yu, J.-X. Sun and Y.-H. Zhou, *Solid State Sciences*, 2010, **12**, 1786-1790.
54 54. A. Samanta, T. Pandey and A. K. Singh, *Phys. Rev. B*, 2014, **90**, 174301.
55 55. C. Y. Fong and M. L. Cohen, *Phys. Rev. B*, 1972, **5**, 3095-3101.
56

Journal Name

ARTICLE

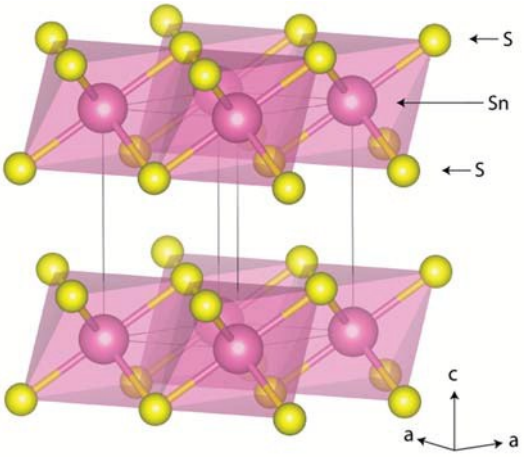

Fig. 1. Layered atomic structure of SnS_2.

Table 1. Selected crystal structure data at the 14 different pressure conditions explored. The refined space group was $P\bar{3}m1$ for the entire pressure range.

p (GPa)	*a* (Å)	*c* (Å)	*V* (Å^3)	z(S)	*d*(Sn-S) (Å)	*d*(S…S) (Å)	∠(Sn-S-Sn) (°)
0.0001	3.6456(4)	5.8934(11)	67.83(2)	0.2473(3)	2.5601(11)	3.647(3)	90.80(7)
0.664(9)	3.6390(3)	5.7853(19)	66.35(2)	0.2513(15)	2.555(5)	3.563(10)	90.82(16)
1.109(11)	3.6339(2)	5.7322(17)	65.56(2)	0.2544(16)	2.555(6)	3.511(11)	90.65(18)
1.991(16)	3.6215(3)	5.650(3)	64.18(3)	0.2565(14)	2.544(5)	3.456(9)	90.76(17)
3.40(3)	3.6067(3)	5.544(2)	62.46(3)	0.2631(14)	2.542(5)	3.352(9)	90.36(15)
4.22(3)	3.5983(4)	5.494(3)	61.61(3)	0.2639(10)	2.533(4)	3.324(7)	90.50(13)
6.29(5)	3.5766(4)	5.393(3)	59.74(3)	0.2701(13)	2.527(5)	3.227(8)	90.09(14)
8.08(6)	3.5605(4)	5.317(3)	58.37(3)	0.2729(16)	2.516(5)	3.171(10)	90.07(16)
9.78(8)	3.5455(3)	5.257(3)	57.23(3)	0.2738(18)	2.502(6)	3.138(11)	90.21(17)
11.88(9)	3.5388(3)	5.157(2)	56.13(3)	0.2775(15)	2.497(5)	3.079(9)	90.23(15)
13.68(19)	3.5362(4)	5.100(3)	55.23(3)	0.2836(15)	2.502(5)	3.007(8)	89.93(15)
14.8(2)	3.5343(4)	5.068(3)	54.82(3)	0.2839(12)	2.497(4)	2.994(7)	90.11(13)
16.8(4)	3.5272(4)	5.026(3)	54.16(3)	0.2859(17)	2.492(5)	2.963(9)	90.08(16)
20(1)	3.5074(7)	4.978(4)	53.05(5)	0.2879(19)	2.481(6)	2.926(10)	89.97(17)

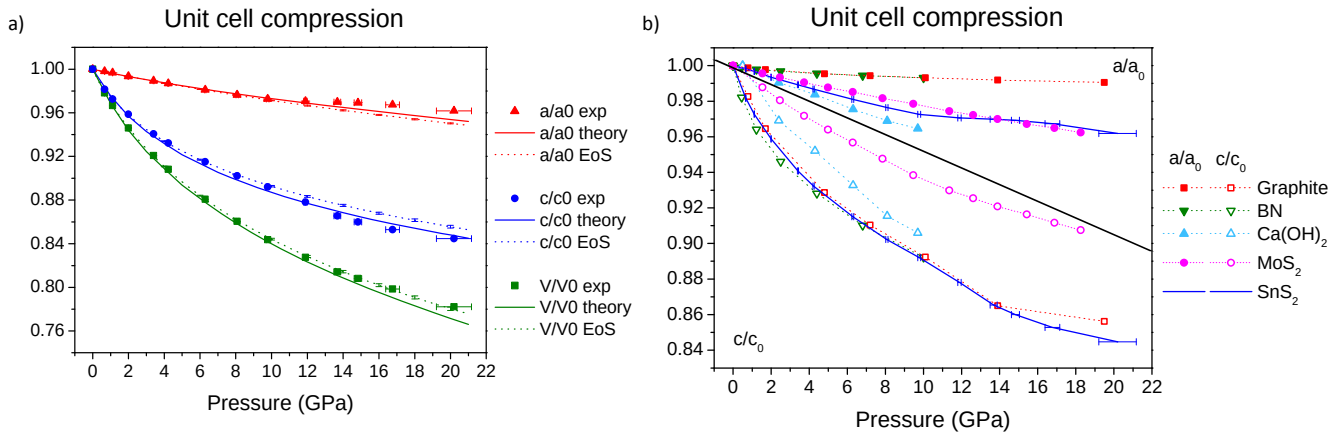

Fig. 2 a) Relative change in unit cell parameters as a function of pressure. Results from theoretical calculations and an equations-of-state fit to data with p < 9.5 GPa have been included, see text for details. b) Comparison of the axis compression of SnS_2 with the compression of the layered structures graphite,[39] BN,[39] $Ca(OH)_2$,[43] and MoS_2.[40]

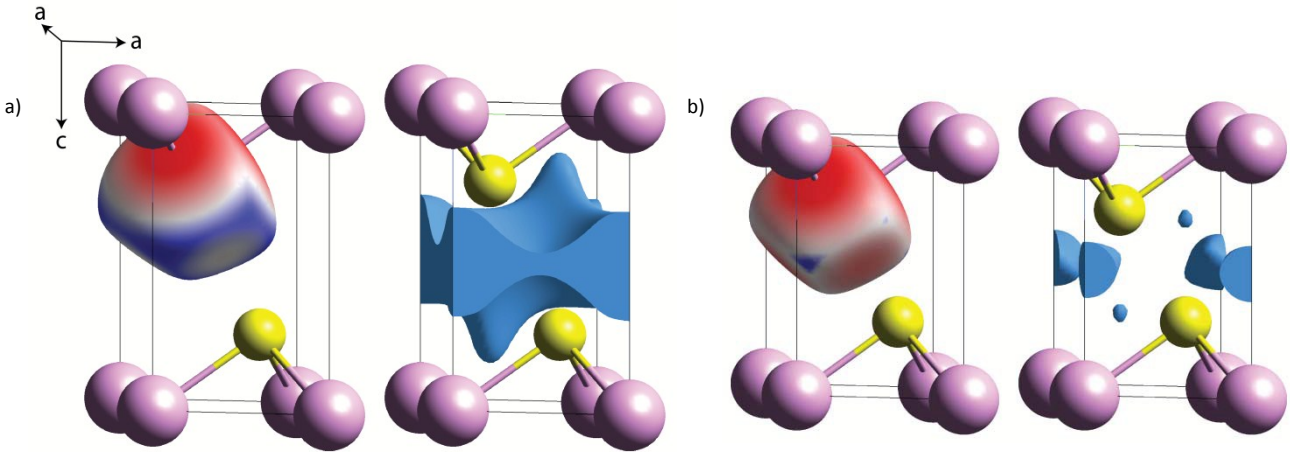

Fig. 3 Illustration of the short contacts to sulfur and the compression of the unit cell by the program CrystalExplorer at a) 0.664(9) GPa and b) 20(1) GPa. Atoms are Sn (pink) and S (yellow). The Hirshfeld surface is mapped with d_{norm}. The blue isosurface visualizes the area of the unit cell, where ρ_{pro} = 0.010 au.

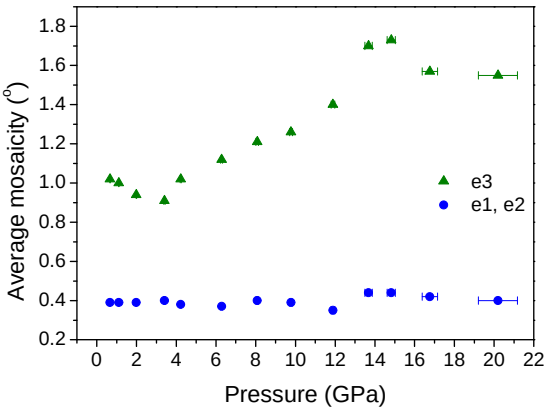

Fig. 4 Average mosaicity as a function of pressure as estimated during integration in SAINT; e1, e2 corresponds to mosaicity in the xy-plane, while e3 corresponds to mosaicity in z.

Table 2. Values from the Birch-Murnaghan equation of state fits to volume and axis compression, respectively. K_0 and M_0 correspond to the bulk modulus from the volume compression and axis compression fits, respectively. *M' is fixed in the 2nd-order refinement of a. Values from studies by Hazen and Finger[18] and Knorr *et al.*[19] are included.

V_0 (Å)	K_0 (GPa)	K'	-	K_0 (GPa)[18]	K_0 (GPa), K'[19]
67.82(2)	28.1(6)	9.5(4)	-	-	exp: 27.9(9), 10.7(7) calc: 28.4(7), 10.5(5)
a_0 (Å)	M_0 (GPa)	M'	$\beta_0(\|\|)$ (GPa^{-1})	$\beta_0(\|\|)$ (GPa^{-1})[18]	$\beta_0(\|\|)$ (GPa^{-1})[19]
3.6468(5)	289(5)	12.00*	$3.46(6)\cdot10^{-3}$	$6.00\cdot10^{-3}$	exp: $2.2(4)\cdot10^{-3}$ calc: $2.4\cdot10^{-3}$
c_0 (Å)	M_0 (GPa)	M'	$\beta_0(\perp)$ (GPa^{-1})	$\beta_0(\perp)$ (GPa^{-1})[18]	$\beta_0(\perp)$ (GPa^{-1})[19]
5.8930(14)	31.5(8)	18.4(7)	$3.17(8)\cdot10^{-2}$	$3.500\cdot10^{-2}$	exp: $2.5(5)\cdot10^{-2}$ calc: $2.85\cdot10^{-2}$

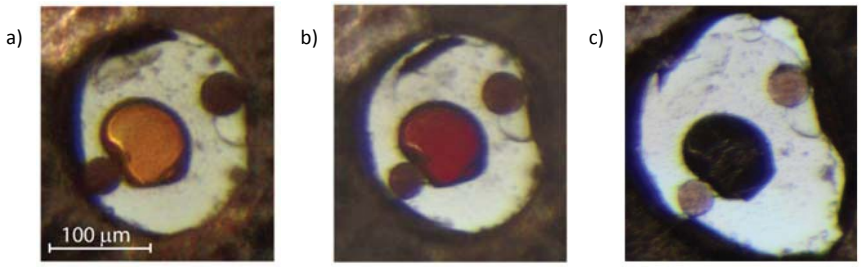

Fig. 5. Images of the crystal at three different pressures: a) 0.66(1) GPa, b) 8.1(1) GPa, c) 16.8(4) GPa. Length scale for all images is indicated in a). Deformation of the steel gasket can be observed.

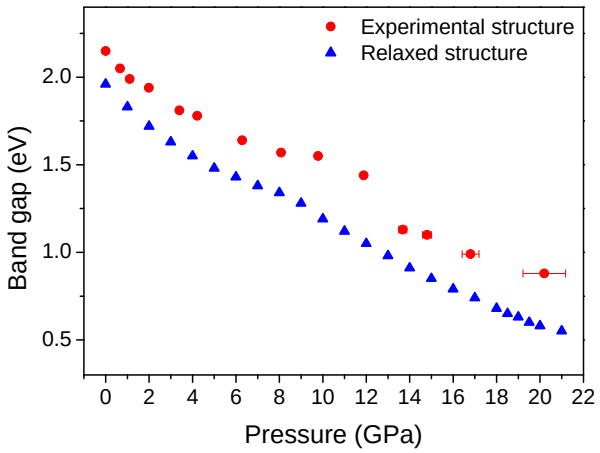

Fig. 6: Indirect band gap as a function of pressure from calculations based on the experimentally determined structure and the relaxed structure.

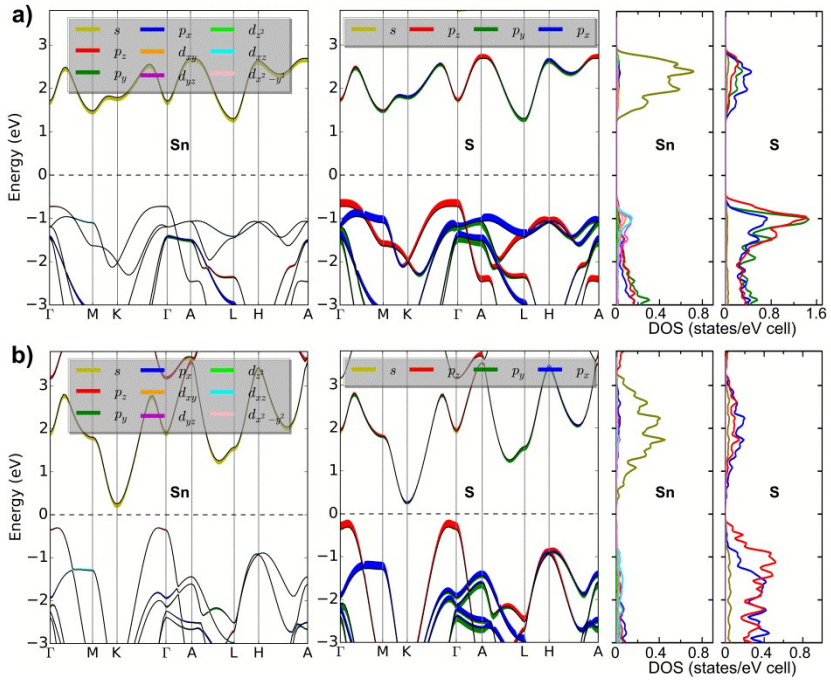

Figure 7. SnS_2 orbital-projected band structure dispersions and density of states at a) 0 GPa and b) 21 GPa. Band widths indicate the relative magnitude of each contribution to the band structure. The curves are normalized according to the core level energies.

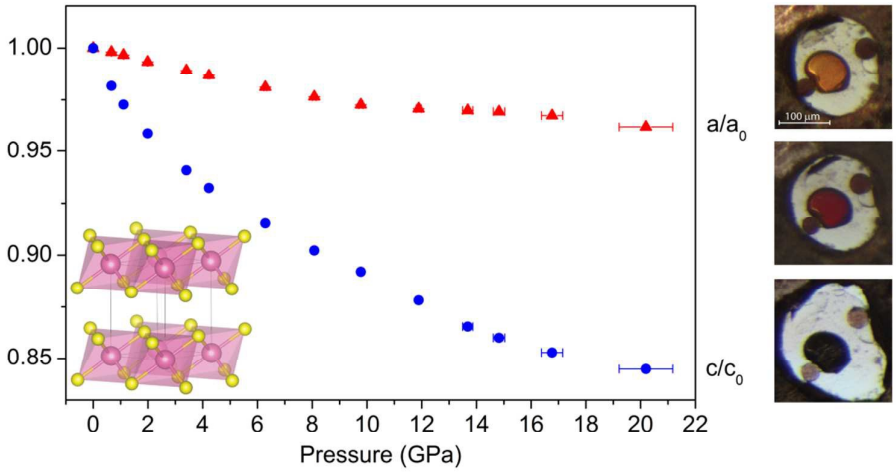

SnS_2 is observed to have a layer compressibility similar to that of graphite, and a reversible color change with pressure is explained from band structure calculations.